

Quasi-two-dimensional quantum states of H₂ in stage-2 Rb-intercalated graphite

A. P. Smith* and R. Benedek

Materials Science Division, Argonne National Laboratory, Argonne, Illinois 60439

F. R. Trouw

Intense Pulsed Neutron Source Division, Argonne National Laboratory, Argonne, Illinois 60439

M. Minkoff

Mathematics and Computer Science Division, Argonne National Laboratory, Argonne, Illinois 60439

L. H. Yang

Physics/H-Division, Lawrence Livermore National Laboratory, University of California, Livermore, California 94551

(Received 6 November 1995)

Inelastic-incoherent-neutron scattering can be a valuable nanostructural probe of H₂-doped porous materials, provided the spectral peaks can be interpreted in terms of crystal-field-split hydrogen-molecule energy levels, which represent a signature of the local symmetry. Inelastic-neutron-scattering measurements as well as extensive theoretical analyses have been performed on stage-2 Rb-intercalated graphite (Rb-GIC), with physisorbed H₂, HD, and D₂ [composition C₂₄M(H₂)_x, with $x = 0.8$ or 1.0], a layered porous system with abundant spectral peaks, to assess whether the crystal-field-state picture enables a quantitative understanding of the observed structure. The experiments were made at 15 K on the QENS spectrometer at the intense pulsed neutron source. Potential-energy surfaces for molecular rotational and translational motion (parallel and perpendicular to the intercalant plane), as well as the intermolecular interactions of hydrogen molecules in Rb-GIC, were calculated within local-density-functional theory (LDFT). A $\sqrt{7} \times \sqrt{7}$ periodic unit cell (with composition C₂₈Rb) was treated in the calculations. Model potentials, parametrized using results of the LDFT calculations, were employed in schematic calculations of rotational and translational excited state spectra of a single physisorbed H₂ molecule in Rb-GIC. Results of our analysis are basically consistent with the assignment by Stead *et al.* of the lowest-lying peak at 1.4 meV to a rotational-tunneling transition of an isotropic hindered-rotor oriented normal to the planes, but indicate a small azimuthal anisotropy and a lower barrier than for the isotropic case. A peak of low intensity at 4.0 meV is most likely a host feature. Based on the experimental isotope shifts and the theoretically predicted states, we conclude that spectral peaks at 11 and 22 meV are most likely related to center of mass excitations. We attribute the relatively weak peak at 32 meV to a librational excitation, and that at 44 meV to an out-of-plane vibration.

I. INTRODUCTION

Adsorbed or intercalated light atoms such as H and He exhibit quasi-two-dimensional quantum behavior at low temperatures.¹ Stage-2 Rb- and Cs-graphite intercalation compounds (GIC's) with physisorbed ("molecularly adsorbed")² H₂ are of special interest because the excited-state spectroscopy measured by inelastic-incoherent-neutron scattering^{3,4} (IINS) of these systems provides a stringent test for models of the quantum states. Although these materials have received less attention than adsorbate systems,^{5,6} the ternary heavy-alkali-metal GIC's with H₂ can provide important insights into quantum behavior in two dimensions, and into the extent to which IINS spectroscopy of hydrogen in porous media can be employed as a local structural probe.

In earlier work^{3,4} the IINS spectra for H₂ in stage-2 Rb- and Cs-GIC were interpreted in terms of a crystal-field-state picture. The direct evidence in support of this model, however, is limited. Improvements in both experimental and theoretical capabilities motivated the present effort to assess more quantitatively the crystal-field-state picture. New high-resolution IINS measurements on H₂ in Rb-GIC were made

at the Intense Pulsed Neutron Source, Argonne National Laboratory, and fill in an energy range missing in the previous work, as well as provide better resolution overall. These results include measurements for HD and D₂ as well as H₂. Furthermore, extensive theoretical calculations were performed within the local-density-functional-theory (LDFT) framework of the potential-energy surface of hydrogen molecules in the Rb-GIC system. These potential surfaces were then employed in model calculations of the ground and excited states for isolated hydrogen molecules in this material, which enable a critical assessment of the origin of the spectral peaks. The basic result of our investigation is that all of the peaks can be interpreted within the crystal-field-state picture, but their positions are in several cases shifted from those predicted with our LDFT potentials. The possible role of intermolecular interactions, neglected in our model calculations, is at present unclear.

Of some general interest is the use of hydrogen-molecule-dopant IINS spectroscopy as a local structural probe of porous structures. The IINS spectrum in principle provides a detailed signature of the local environment in the vicinity of the site occupied by the molecule. Hydrogen molecules have

been proposed as probes of local structure in other porous systems, such as molecular sieves.⁷ This approach can be successful only if a relatively simple interpretation exists of the excited states. Our analysis of Rb-GIC, with a key role played both by the measurements for several isotopes and the *ab initio* calculations, provides some hope that this can actually be accomplished.

A brief description of the atomic structure of Rb-GIC as it bears on the ternary system with absorbed hydrogen is given in Sec. II. This is followed in Sec. III by a description of the IINS experiments, as well as a summary of previous measurements on these materials. The theory is presented in Sec. IV. An interpretation of the spectral peaks is given in Sec. V. A summary appears in Sec. VI.

II. HEAVY-ALKALI GIC WITH PHYSISORBED HYDROGEN

In the heavy-alkali-metal (Rb or Cs) GIC's with physisorbed hydrogen molecules, the molecular center-of-mass motion is essentially confined to a plane midway between two graphene sheets, whose separation is stretched from 3.35 Å in pristine graphite to 5–6 Å in the intercalated system by the heavy-alkali-metal atoms. Calculations described in Sec. IV confirm the steep energy barriers to molecular center-of-mass motion perpendicular to the layers. Since the molecular center-of-mass motion in the intercalant plane is relatively free, this material can be regarded as a kind of atomic quantum-well system. Owing to the large “gallery” width, the H₂ molecular bond length and vibrational frequency are virtually unchanged from their values in vacuum.⁸ Judging by the behavior of rare-gas adsorbates on graphite, the intermolecular interaction is also expected to have similar form to that in vacuum, with a slightly shallower attractive potential well.⁹

Since the molecule is undissociated in stage-2 GIC, it has orientational as well as center-of-mass degrees of freedom. In contrast to adsorbed H₂ on graphite,¹⁰ the low-energy orientation of adsorbed molecules is perpendicular to the layers, as a consequence of quadrupolar interactions with alkali-metal-atom intercalants, as described in Sec. IV. The molecular intercalates exist only in stage 2 (two graphene sheets separate successive intercalant layers), but not in the more densely intercalated stage 1, with composition C₈M. A complicating feature of the stage-2 heavy-alkali-metal GIC, with approximate stoichiometry C₂₄M, is its incommensurate intercalant structure and the resultant disordered crystal potential. Periodic intercalant structures that consist of $\sqrt{7} \times \sqrt{7}$ domains separated by grain boundaries have been proposed^{11–13} as approximants to the actual disordered structures. The picture of the intercalant structure as a mosaic of small $\sqrt{7} \times \sqrt{7}$ domains is supported by molecular-dynamics simulations.^{14,15}

Hydrogen can dope the stage-2 heavy-alkali GIC's continuously, up to slightly greater than two molecules per alkali-metal intercalant; however, the phase diagram is unknown. A reconstruction appears to occur in the vicinity of 0.8 molecules per alkali-metal atom. X-ray diffraction measurements¹⁶ would be useful to determine whether the reconstruction involves the host or only the hydrogen dopants.

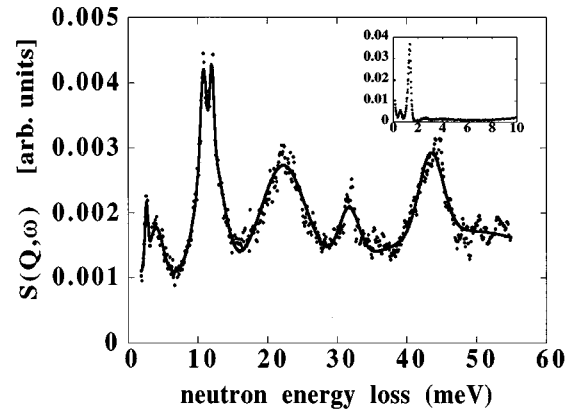


FIG. 1. Inelastic-neutron-scattering spectrum for the ternary GIC C₂₄Rb(H₂)_{1.0} at 15 K measured on QENS spectrometer at IPNS, Argonne National Laboratory. The inset shows the rotational tunneling peak at 1.4 meV. The solid line represents a fit to the data with Gaussians.

III. EXPERIMENT

A. Previous work

Previous inelastic-incoherent-neutron-scattering measurements were performed by Stead *et al.*^{3,4} at Institut Laue-Langevin and on the DIDO beryllium-filter spectrometer at Harwell for both stage-2 Rb- and Cs-GIC [C₂₄M(H₂)_x] at various hydrogen-molecule fillings, *x*. Measurements were also made on specimens doped with HD. The lowest peak energy (≈ 1.4 meV for specimens with H₂) was independent of filling for $x < 0.8$. This peak was identified as the rotational-tunneling transition¹⁷ for a molecule located at “site A” within the intercalant plane. At higher fillings, $2 > x > 0.8$, a new set of peaks identified with “site B” transitions appear,^{3,4} well removed in energy from those of site A. Furthermore, the line shapes of the site A peaks are modified. The energies of several of the observed features, including the rotational-tunneling peak and some higher-lying peaks, were found consistent with predictions of the isotropic hindered-quantum-rotor model.^{3,4}

B. Present measurements

Although Stead *et al.*^{3,4} investigated these systems in considerable detail, the important energy interval 5–15 meV was omitted from their measurements owing to instrumental limitations. To obtain more complete and higher-resolution data, particularly in the energy range below about 20 meV, spectra were measured for C₂₄Rb(H₂)_x with the QENS spectrometer at the Intense Pulsed Neutron Source, Argonne National Laboratory. Measurements were also made on HD and D₂ to determine the mass dependence of the spectra, as described below. Polycrystalline specimens¹⁸ were prepared with fillings $x = 0.8$ or 1.0. Neutron final energy was fixed at 3.65 meV.

The IINS spectral intensity at energies below 55 meV measured at 15 K (Ref. 19) for hydrogen-molecule filling $x = 1.0$ is shown in Fig. 1. The solid curve represents a fit to the data (based on a superposition of Gaussians), and the inset highlights the rotational-tunneling transition at 1.4 meV, the highest intensity feature in the spectrum. We note

that at least three of the peaks that appear in Fig. 1 (i.e., those at 2.7, 11, and 22 meV) cannot be accounted for within the isotropic hindered-rotor model.^{3,4} The split peaks at 2.7 and 11 as well as the peak at 32 meV were not observed in the earlier work.^{3,4} Although well-defined higher energy transitions may exist, our measurements show no distinct peaks at energies above those shown in Fig. 1.

C. Isotope shifts

Measurements were made on Rb-GIC specimens doped with HD and D₂ as well as H₂. No previous work on D₂ has been published. Results are shown in the three panels of Fig. 2. Some of the more prominent peaks are indicated by vertical lines at the top of each panel. The peak energies are listed in Table I. Peak energies that (hypothetically) belong to corresponding states are listed on the same row of the table. Ratios of HD and D₂ energies to those for corresponding H₂ transitions are also listed. For reference, inverse-square-root mass scaling gives a ratio 0.82 for HD/H₂ and 0.71 for D₂/H₂, whereas inverse mass scaling give a ratio 0.67 for HD/H₂ and 0.5 for D₂/H₂. The isotopic shifts for the corresponding-peak assignments shown in the table follow very closely the prediction of inverse-square-root scaling for the transitions at 10.7, 11.9, 22.1, and 43.7 meV for H₂.

For a translational degree of freedom governed by a power-law potential $V(x)=Cx^n$, the energy eigenvalues scale with mass as $m^{-n/(n+2)}$. For rotational degrees of freedom or most other types of translational potentials, on the other hand, no comparably simple isotopic scaling exists. The inverse-square-root scaling found for the 11, 22, and 44 meV peaks may therefore plausibly be attributed to harmonic oscillator potentials. Note that a flat potential with hard boundaries (i.e., a square-well potential) would result in inverse-mass scaling.

D. Para- and orthohydrogen

To interpret the spectra properly, the relative population of ground and first excited hydrogenic states in the measured specimen must be known. If the lowest-lying excited state ($E_{H_2}=1.4$ meV) is associated with rotational tunneling, then para (p) and ortho (o) correspond to the ground (g) and excited (e) states, respectively, in the specimen filled with H₂. At equilibrium, the Boltzmann population ratio

$$o/p = e/g = 3 \exp(-E_{H_2}/kT). \quad (1)$$

At $T=15$ K, $o/p \approx 1$. Close agreement between spectra measured before and after a two-week holding period (at low temperature) indicates that the ortho-para ratio was close to equilibrium. In the case of HD, $e/g = \exp(-E_{HD}/kT)$ and for D₂, $e/g = (1/3)\exp(-E_{D_2}/kT)$. The lowest excited level in HD, $E_{HD}=0.45$ meV (see Table I), and the corresponding equilibrium population ratio at 15 K $e/g \approx 0.7$, of similar magnitude to that for H₂. Therefore, even at 15 K, e/g is of order unity for either HD or H₂ filling.

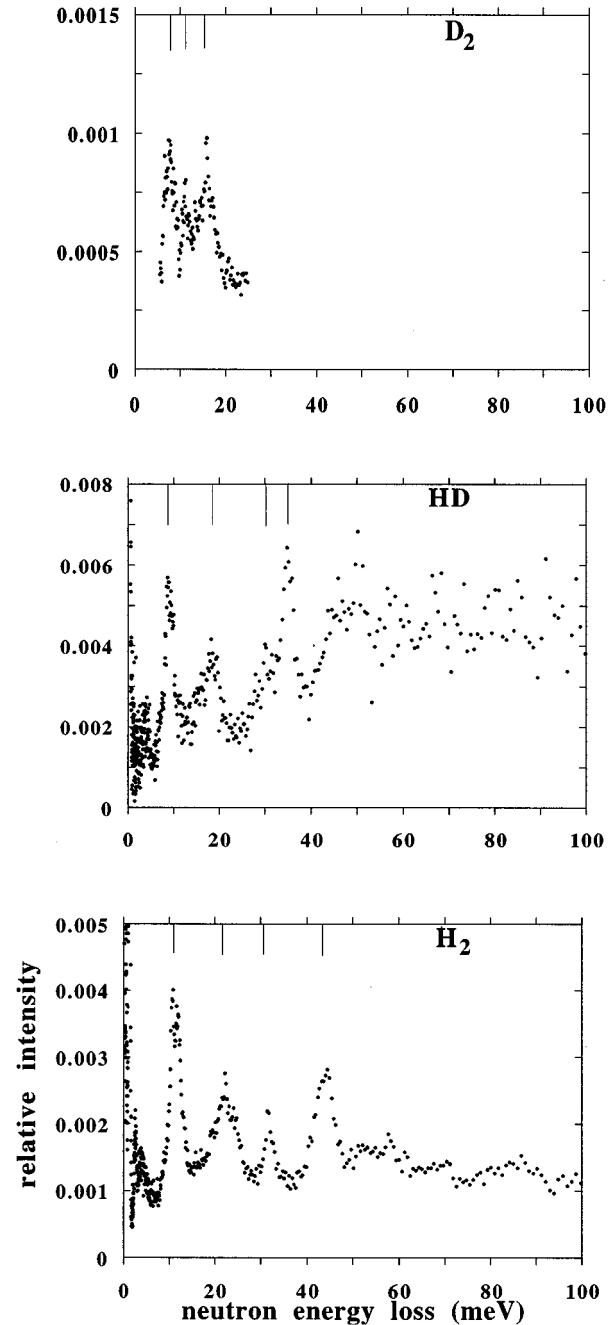


FIG. 2. Inelastic-neutron-scattering spectra for the ternary GIC $C_{24}Rb(H_2)_x$ at 15 K measured on QENS spectrometer, Argonne National Laboratory. The panels show results for D₂ ($x=0.8$), HD ($x=0.8$), and H₂ ($x=1.0$), respectively. Vertical lines at top of each panel indicate peak positions.

IV. THEORY

The sharply structured IINS spectrum (Fig. 1) suggests that the ground and low-lying excited molecular states have identifiable physical interpretations. The abundance of spectral peaks makes $C_{24}Rb(H_2)_x$ particularly challenging to theory. Stead *et al.* interpreted their results in terms of localized crystal-field molecular states, a reasonable hypothesis in view of the proportionality of the peak intensities and the insensitivity of their positions to hydrogen filling (for $x < 0.8$).³ The localized-crystal-field-state picture underlies

TABLE I. Observed transition energies (meV) for H_2 , HD, and D_2 , and ratios of transition energies in HD and D_2 to corresponding energies in H_2 . Peak widths (half-width at half maximum) and relative areas are also noted for the H_2 peaks.

Position	H_2 Width	Area	HD Position	HD/ H_2 Ratio	D_2 Position	D_2/H_2 Ratio
1.4	0.1	1	0.4	0.29		
2.7	0.3	0.1				
4.0	1.5	0.25				
10.7	1	1	8.8	0.82	7.7	0.72
11.9	1	1	9.6	0.81		
22.1	3.5	1	18.3	0.83	15.6	0.71
31.7	1.5	0.25	30.1	0.95		
43.7	2.5	1	34.9	0.80		

the “site A(B)” nomenclature and the corresponding site-population analyses presented in the earlier work.³ Calculations^{3,4} based on an azimuthally symmetric hindered-rotor model, furthermore, suggest that some of the peaks are attributable to rotational transitions. The remaining (nonhost) peaks may plausibly be identified with excited states of the molecular center-of-mass motion.

In spite of its plausibility, however, evidence for the localized-crystal-field-state picture is inconclusive, and more detailed tests are required to establish its validity. In this section, we calculate the excited-state spectra of the molecules, at least schematically, to facilitate such tests. Calculation of the molecular states requires knowledge of the molecule-host interaction, the subject of Sec. IV A below. In the present calculations, the host electrons are treated within the Born-Oppenheimer approximation, and the host lattice is treated as static. Excitation energies are therefore treated within the Franck-Condon approximation. A periodic approximant to the host structure is considered in calculations of electronic structure and total energies. Furthermore, intermolecular interactions are neglected. Although none of these approximations is insignificant, the present single-particle framework is a necessary starting point. Since the quantum states of light interstitials in metals require a many-body description even in the simplest cases,^{20–22} one might be inclined to dismiss the present anisotropic and disordered system as intractable theoretically. Nevertheless, the experimental fact of abundant and sharp IINS peaks, which in many materials are not observed, suggests that clear interpretations are available.

A difficult theoretical issue is the extent of localization of the hydrogen molecules. In general, several factors will tend to localize the ground state and to a lesser extent excited states, including the quasi-two-dimensionality of the system,²³ the disordered intercalant structure of the host,²⁴ self-trapping,²⁵ and coupling to host phonons,²⁰ electronic effects beyond the Born-Oppenheimer approximation,²¹ and intermolecular interactions. The H_2 single-particle potential in stage-2 Rb GIC, discussed below, is not strong enough in itself to localize excited states at many of the observed IINS peak energies. Strong localization either of the ground or excited states is, however, not strictly required to produce sharp IINS peaks.²⁶

A. Interatomic potentials

The components of the H_2 interaction potential are discussed in this section. Following a progression of descending

energy scales, the out-of-plane translational potential will be considered first, then the rotational and the translational potentials of isolated hydrogen molecules, and finally the intermolecular interaction.

Previous calculations for adsorbates on clean¹⁰ and rare-gas-plated²⁷ graphite employed model pairwise and three-body interactions.²⁷ The interatomic interactions of hydrogen molecules in stage-2 Rb GIC, however, has not received previous attention. Our construction of pairwise potentials is guided by LDFT total-energy calculations. We find that within the intercalant plane, the H_2 -alkali interaction dominates the H_2 -graphite (“corrugation”) potential. Furthermore, the energy scale for H_2 perpendicular vibrations is, as expected, higher than that for in-plane motion. Physically, the H_2 -alkali-atom potential represents the superposition of a screened quadrupole-quadrupole interaction at intermediate range and a core-overlap repulsion at short range. The strength of the attractive quadrupolar interaction is determined by the charge transfer of the H_2 and the Rb intercalants to the graphite layers and by the dielectric properties of the layers. An analysis of charge transfer indicates that the electropositive alkali-metal intercalants donate most of their valence charge to the graphene sheets,²⁸ whereas the adsorbed molecules are slightly electronegative, thereby leading to a weak Coulomb attraction between the hydrogen molecule and alkali-metal atom.

1. Local-density-functional-theory calculations

The potential-energy surface of hydrogen molecules was obtained from LDFT total-energy calculations for a periodic system with composition $C_{28}RbH_2$. LDFT is the best available approach, since correlated many-electron-wavefunction techniques would be computationally prohibitive. The present application, nevertheless, poses a severe test of the LDFT methodology, owing to the small energy scales, the anisotropy in the layered GIC system, and the possible importance of exchange and correlation contributions, which LDFT treats only in a local approximation.

A plane-wave basis with a cutoff energy of 60 Ry, and separable norm-conserving pseudopotentials of the Troullier-Martins²⁹ form, were employed. The semicore 4p electrons of Rb, which lie within the graphite valence band, are treated as band states.^{30,31} Self-consistent Kohn–Sham orbitals were obtained by a preconditioned conjugate-gradient method algorithm,³² modified to treat metallic

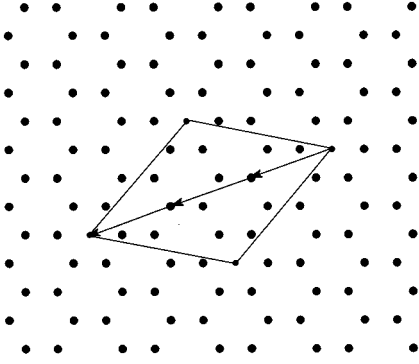


FIG. 3. Large circles denote the carbon honeycomb lattice, and small circles represent alkali-metal-ion intercalant positions in the C₂₈Rb unit cell. Lines terminating on arrows illustrate generating vectors for the P3 polytype. These vectors represent the in-plane translation of one intercalant layer relative to an adjacent layer. (The two graphene sheets that sandwich each intercalant layer are translated by one-third the second-nearest neighbor honeycomb-lattice spacing, relative to the adjacent sandwiches.) After three translations, the sequence repeats itself. The P3 polytype corresponds to the largest generating vector; two smaller generating vectors correspond to polytypes P21a and b.

systems.³³ The Gaussian-broadened method³⁴ was employed, with four special k points.

The $\sqrt{7} \times \sqrt{7}$ supercell of the graphite honeycomb lattice, a commensurate-approximant to the alkali-metal-intercalant structure, which corresponds to composition C₂₈Rb, was chosen as the periodic unit cell in these calculations. As mentioned above, the actual intercalant structure is a disordered mosaic of commensurate $\sqrt{7} \times \sqrt{7}$ domains separated by domain boundaries of higher alkali density. The site-A positions are thought to be located within the $\sqrt{7} \times \sqrt{7}$ domains.³ According to this viewpoint, the present calculations pertain to the site-A spectroscopic features.

To fully specify the unit-cell configuration, stacking sequences for both the graphite and the intercalant layers must be selected. The ideal graphene-layer stacking sequence for stage-2 GIC,³⁵ A|AB|BC|C, where the vertical spacers represent intercalant layers, is employed throughout. Three inequivalent intercalant stacking sequences (polytypes) are compatible with this graphite-layer sequence. The polytypes will be denoted P21a,b and P3, and have repeat lengths of 21, 21, and 3 intercalant layers, respectively. The three polytypes differ in the nearest-neighbor spacings of intercalants in adjacent layers. Since the alkali-alkali interaction is repulsive,³¹ the polytype P3, which has the largest interlayer nearest-neighbor separation, is expected to have the lowest energy. The stacking sequences for the P3 polytype is illustrated in Fig. 3. The arrow indicates the in-plane displacement of a given intercalant layer relative to an adjacent layer. The P21a sequence is generated by a translation vector connecting a hexagon-center position and a hexagon vertex; P21b is generated by a vector twice as large, but with the same orientation. We emphasize that these polytypes pertain only to our idealized periodic system with composition C₂₈Rb, and do not actually occur in nature.

Calculations were performed with either one or two hydrogen molecules per unit cell. The $\sqrt{7} \times \sqrt{7}$ cell with a

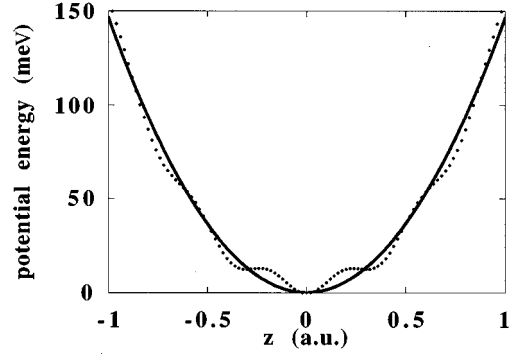


FIG. 4. Potential energy of a hydrogen molecule as a function of the center-of-mass coordinate z perpendicular to the layers. Calculation performed for P21a polytype, with molecular axis oriented normal to layers; in-plane position r described in the text. Solid line represents fit to a parabola.

single hydrogen molecule provides information about potentials in the dilute limit, since the intermolecular interaction is negligible at separations of the order of the lattice constant $\sqrt{21}d = 12.4$ a.u., where d is the carbon-carbon bond length.

Most of the LDFT calculations employed observed lattice constants, although a few calculations were done for LDFT predicted lattice constants.³³ The predicted in-plane lattice constant is about 1% smaller than experiment, whereas the calculated equilibrium c -axis lattice constant is 6% larger than experiment. We have employed for the A|A sandwich thickness the measured c -axis lattice constant of stage-1 Rb-GIC,³⁶ and for the AB spacing the interlayer separation of pristine graphite. C–C bond lengths appropriate to stage-1 Rb GIC (Ref. 36) were employed. The small layer expansion and distortion resulting from the H₂ doping³⁷ are neglected.

LDFT calculations are applied in the following to characterize the crystal potential

$$V(\mathbf{r}, z, \Omega), \quad (2)$$

of an H₂ molecule embedded in a stage-2 Rb GIC matrix. Here \mathbf{r} and z are the molecular center-of-mass coordinates parallel and perpendicular to an intercalant layer, and $\Omega = (\theta, \phi)$ represents the molecular orientation; the H₂ bond length⁸ is treated as fixed. The slight buckling of the graphene sheets resulting from intercalation³⁸ is neglected in the calculations.

2. Out-of-plane center-of-mass potential

The potential for translations in the z direction, perpendicular to the layers, is illustrated in Fig. 4. The plotted results correspond to the P21a polytype, $\theta=0$ and \mathbf{r} located slightly displaced from a trigonal site (trigonal sites are equidistant from three intercalants in the $\sqrt{7} \times \sqrt{7}$ supercell) along a line joining the trigonal to an alkali-metal intercalant site; this is a relatively low-energy in-plane position, as will be seen below. A quadratic potential $V = kz^2/2$ fitted to the calculated points is represented by the solid curve. The calculated points oscillate about this best-fit harmonic potential. Based on the curvature k , we find the energy scale for perpendicular center of mass motion of hydrogen molecules is of order $\hbar\omega = 45$ meV. Perpendicular vibrations therefore

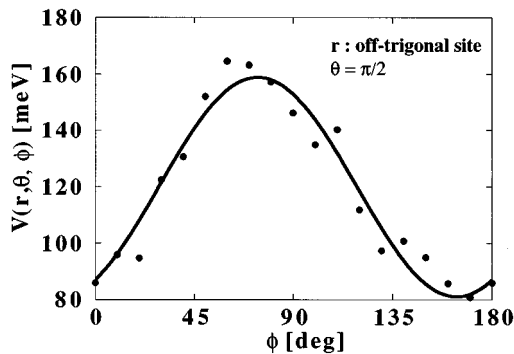


FIG. 5. Azimuthal-angle dependence of the rotational potential for r in off-trigonal site (see text), with the molecular axis parallel to the layers.

possess a higher energy scale than many of the excitations that appear in the IINS spectrum (Fig. 1). The out-of-plane potential-energy curve varies only moderately with in-plane position \mathbf{r} ; for example, results for the trigonal site are almost identical to those for the off-trigonal site plotted in Fig. 4 for z less than 0.5 a.u. The zero-point molecular-center-of-mass vibrational amplitude normal to the layers is approximately 0.3 a.u. For comparison, the vibrational (rms) amplitude perpendicular to the layers of bulk graphite at low temperatures³⁹ is 0.12 a.u.

3. Rotational potential

Rotational spectra were analyzed by Stead *et al.*^{3,4} with an isotropic-hindered-rotor model, where the rotational-energy barrier was treated as an unknown parameter. The present LDFT calculations essentially confirm the validity of this model, generalized slightly to include a small azimuthal-angle anisotropy in the rotational barrier.

Three different center-of-mass positions, \mathbf{r} , were examined, the trigonal site, the “bridge” position midway between two nearest-neighbor alkalis, and a site about 20% of the distance from a trigonal to an intercalant site. The polar-angle energy dependence is well represented in all cases by $V(\theta) \sim 1 - \cos(2\theta) = 2 \sin^2\theta$, with the preferred molecular orientation ($\theta=0$) parallel to the c axis. The azimuthal-angle dependence is given approximately by $V(\phi) \sim a + b \cos(2[\phi - \phi_0])$, where the anisotropy amplitude b/a is essentially zero at the trigonal site, 0.32 at the off-trigonal site, and 0.40 at the bridge site. The calculated results for the off-trigonal site are plotted in Fig. 5, along with a fit (solid curve) to the analytical form. The mean energy barrier for rotation through the equatorial plane ($\theta = \pi/2$), $a = 96, 120,$ and 121 meV for the trigonal, off-trigonal, and bridge sites, respectively. Although results are mentioned only for the P21a polytype, similar behavior would be expected for the other two polytypes.

4. In-plane center-of-mass potential

The center-of-mass motion of the molecule is governed primarily by the potential $V(\mathbf{r}, z=0, \theta=0)$. As mentioned above, quadrupolar interactions between a H_2 molecule and an alkali-metal intercalant tend to align it normal ($\theta=0$) to the layers. In addition to the quadrupolar interaction, the cen-

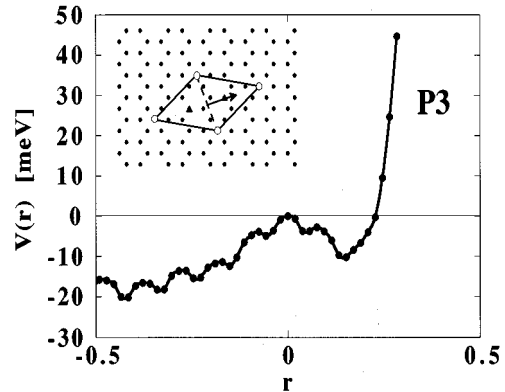


FIG. 6. Center-of-mass potential for H_2 along a slice (indicated by the line with the arrow) through the unit cell starting at a bridge site ($r = -0.5$) and passing through a trigonal site ($r = 0$). The potential becomes steeply repulsive as an alkali-metal-atom intercalant site at $r = 1.0$ is approached. Trigonal sites are indicated by triangles. The plotted results are for the P3 polytype.

ter of mass potential also includes a corrugation potential resulting from interactions with the graphene sheets, interactions with alkali-metal ions in other layers, and intermolecular interactions. Within the present treatment, the center-of-mass potential possesses the periodicity of the chosen $\sqrt{7} \times \sqrt{7}$ unit cell. The $\sqrt{7} \times \sqrt{7}$ unit cell is illustrated by solid lines in the inset to Fig. 6. The dashed line divides the cell into two equilateral triangles whose vertices are occupied by Rb intercalants; the center-of-mass potential of a single H_2 molecule must be determined only within one of these symmetrically equivalent triangles. The filled triangles denote trigonal positions at the center of the irreducible triangles. The results plotted in Fig. 6 represent the potential along a line from a bridge site ($r = -0.5$, in units of the alkali-metal ion-trigonal site separation $\sqrt{7}d_{CC}$, where d_{CC} is the carbon-carbon bondlength) through a trigonal site ($r = 0$, filled triangles in the inset) toward an alkali-metal ion ($r = 1.0$). These results correspond to the P3 polytype; the P21 polytype is considered below.

We note first that the energy scale (~ 20 meV) is indeed lower than that for the rotational potential. Going from the trigonal site $r = 0$ (which we arbitrarily set as the energy zero) in the $+r$ direction, $V(r)$ shows an attractive region with a minimum near $r = 0.15$, owing to the attractive quadrupolar interaction, followed by a sharply repulsive core-overlap region as the molecule approaches the Rb intercalant. The van der Waals radii (1.2 Å for H_2 , and 1.49 Å for Rb^+) touch at $r = 0.29$, where the potential is already strongly repulsive. In the opposite direction, toward the bridge site at $r = -0.5$, the molecule experiences the attractive quadrupolar interaction with both members of the bridge, while avoiding the core overlap, since the bridge length, 6.55 Å, is larger than the sum of van der Waals diameters. These calculations were based on experimental values of the lattice parameters, which, as mentioned, differ from the equilibrium values determined from LDFT calculations. To test the sensitivity of the results to the lattice constants, calculations were also performed for the calculated equilibrium lattice constants.³³ The results were similar to

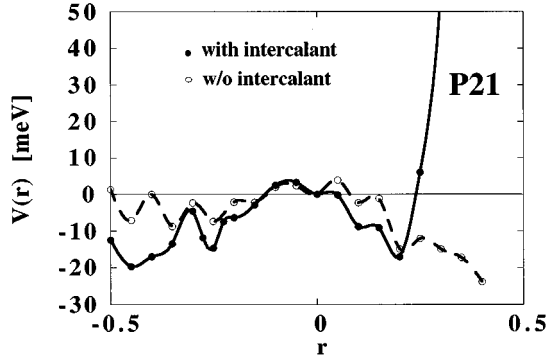


FIG. 7. Center-of-mass potential for H₂ along the same path as in previous figure for the P21a polytype. The points are on a coarser grid than in Fig. 6.

those shown in Fig. 6, but with a slightly shallower minimum near $r=0.15$.

The center-of-mass potential for the P21a polytype is plotted in Fig. 7 (solid curve); these results are analogous to those for the P3 polytype plotted in Fig. 6. Apart from fine-scale oscillations, the overall structure of the potential for the two polytypes is similar. Fine scale oscillations with a period of about $0.1(\sqrt{7}d)$ appear in both cases. It is tempting to attribute these oscillations to the graphite corrugation potential, but they are most likely a numerical artifact associated with the FFT grid.

To represent the potential throughout the unit cell, it is convenient to express the energy in terms of an effective molecule-alkali-metal-atom central-force pair potential. We have employed a parametrized potential of the form

$$V_2(x) = A \exp(-\alpha[x-x_0]) - C/x^4 + D/x^8, \quad (3)$$

where $x \equiv 1 - r$ is the hydrogen molecule-Rb separation, the potential minimum $x_0 = 0.84$, and A , α , C , and D are adjustable parameters. Qualitatively, the first term represents the core-overlap repulsion, and the sum of the inverse-power potentials the alkali-metal-atom-hydrogen-molecule (screened) quadrupole interaction. The total potential is then the sum of pairwise interactions with the Rb neighbors of a hydrogen molecule. The parameters⁴⁰ in Eq. (3) were fitted to the calculated results in Fig. 6 between $r=0.0$ and $r=0.3$, with the potential constrained to cut off at $x=1$. The harmonic approximation to this potential has a minimum $E_0 = -8.6$ meV at $x_0 = 0.84$, with corresponding frequency $\hbar\omega_0 = 18.9$ meV for H₂; anharmonicity is therefore pronounced even for the ground state.

5. Intermolecular potential

The effective interatomic interaction between rare-gas adsorbates on graphite is substantially the same as in vacuum.⁹ This is also expected to be the case for the intermolecular interaction of hydrogen intercalated in stage-2 Rb GIC, as mentioned in Sec. II. LDFT total-energy calculations were performed, as a function of intermolecular separation, on a unit cell with two molecules oriented perpendicular ($\theta=0$) to the layers. The molecules are placed symmetrically on opposite sides of a bridge site. Positions of the 28 carbon atoms in

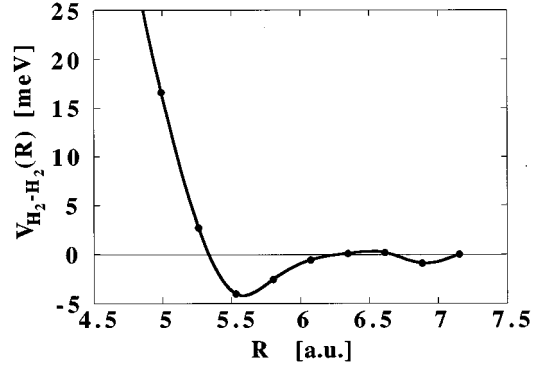


FIG. 8. Effective intermolecular potential for H₂ molecules in stage-2 Rb-GIC, based on Eq. (4). The molecular axes are perpendicular to the layers. R is the distance between the center of mass positions of the two molecules, which are located on opposite sides of a bridge site. Potential zero arbitrarily chosen to correspond to molecules on adjacent trigonal sites.

the unit cell are kept fixed in these calculations. The calculated effective intermolecular potential

$$V_{eff}(R_a, R_b) = E[C_{28}Rb(H_2)_2] - 2E(C_{28}RbH_2) + \text{const}, \quad (4)$$

where R_a and R_b are the center-of-mass positions of the two molecules, is plotted in Fig. 8. The effective potential $V_{eff}(R)$ shows a minimum slightly deeper and at intermolecular separation 1 a.u. smaller than isotropic intermolecular potentials in vacuum.⁴¹ With the molecular orientation assumed in the present calculations, steric hindrance is smaller than in the isotropically averaged interaction, which accounts for the shorter minimum-energy intermolecular separation. The results for $V_{eff}(R)$ indicate that the attractive part of the intermolecular potential is somewhat weaker, but of the same order of magnitude, as that for the H₂-Rb interaction (Fig. 6).

B. Hydrogen-molecule eigenstates

The results presented in Sec. IV A indicate that the in-plane motion has a lower energy scale than the rotational and out-of-plane-vibrational motion. To simplify, we treat the latter degrees of freedom in an adiabatic approximation, so that the in-plane motion is governed by an effective potential in which the rotational and vibrational motion are integrated out. Accordingly, the potential that enters the molecular Schroedinger equation

$$[H(\mathbf{r}, z, \Omega) - E]\Phi = 0, \quad (5)$$

where $H = T + V$, is approximately decomposed into three terms,

$$V(\mathbf{r}, z, \Omega) = u(\mathbf{r}) + v(\mathbf{r}, z) + w(\mathbf{r}, \Omega), \quad (6)$$

with $u(\mathbf{r}) \equiv V(\mathbf{r}, z_0, \Omega_0)$, the in-plane potential; $v(\mathbf{r}, z) \equiv V(\mathbf{r}, z, \Omega_0) - V(\mathbf{r}, z_0, \Omega_0)$, the out-of-plane vibrational potential; and $w(\mathbf{r}, \Omega) \equiv V(\mathbf{r}, z_0, \Omega) - V(\mathbf{r}, z_0, \Omega_0)$, the rotational potential. Here z_0 refers to the intercalant plane, and Ω_0 corresponds to a molecular orientation perpendicular to the layers.

We employ a product wave function

$$\Phi(\mathbf{r}, z, \Omega) = \chi_{J,M}(\mathbf{r}, z_0; \Omega) \xi(\mathbf{r}, \Omega_0; z) \psi(\mathbf{r}) \quad (7)$$

and factor the Schrödinger equation into rotational

$$[h_{rot}(\mathbf{r}, \Omega) - E_{J,M}(\mathbf{r})] \chi_{J,M}(\mathbf{r}, z_0; \Omega) = 0, \quad (8)$$

vibrational

$$[h_{\perp}(\mathbf{r}, z) - E_n(\mathbf{r})] \xi_n(\mathbf{r}, z) = 0, \quad (9)$$

and in-plane

$$[h_{\parallel}(\mathbf{r}) - E_i] \psi_i(r) = 0 \quad (10)$$

components. Here $h_{rot}(\mathbf{r}, \Omega) = t_{rot} + w(\mathbf{r}, \Omega)$, $h_{\perp}(\mathbf{r}, z) = t_{\perp} + v(\mathbf{r}, z)$, and $h_{\parallel}(\mathbf{r}) = t_{\parallel} + V_{\parallel}(r)$, where the in-plane adiabatic potential is

$$V_{\parallel}(r) = u(\mathbf{r}) + E_{00}(\mathbf{r}) + E_0(\mathbf{r}). \quad (11)$$

The foregoing separation of variables, based on Eq. (6), will be employed throughout the remainder of this article. The degrees of freedom \mathbf{r} , z , and Ω are assumed weakly coupled, as a first approximation. We do not present a formal justification of the adiabatic approximation, but to check its plausibility, numerical calculations were performed of the z dependence of the rotational barrier $V(\mathbf{r}, z_0, \Omega_1) - V(\mathbf{r}, z_0, \Omega_0)$, where $\Omega_1 \equiv (\pi/2, \phi)$; the in-plane coordinate, \mathbf{r} , was located at a trigonal site, at which the ϕ dependence is small. Only a gradual decrease of the rotational barrier is found as z is moved away from the intercalant plane z_0 , which indicates that rotational-vibrational coupling is small.

Note also that the H_2 bond length is held fixed, since the associated vibrational frequency is an order of magnitude larger than any of the other energy scales.

1. Rotational eigenstates

The results presented above show that the rotational motion has the largest energy scale of the in-plane degrees of freedom represented in the potential $V(\mathbf{r}, \theta, \phi)$. We found in Sec. IV A 3 an anisotropic hindered-rotor potential

$$w(\mathbf{r}, \Omega) = \sin^2 \theta [a(\mathbf{r}) + b(\mathbf{r}) \cos(2\phi)]. \quad (12)$$

This potential apparently has not been studied previously, although a similar potential with $\cos^2 \theta$ polar-angle dependence has been treated.⁴² To gain insight into the role of azimuthal anisotropy (ϕ dependence), which was neglected in the previous work,⁴ the Schrödinger equation for a quantum rotor in a potential given by Eq. (5) was solved numerically with a spherical-harmonic basis set, Y_{lm} . The method of solution is described briefly in the Appendix. The appropriate dimensionless parameters for the problem are the reduced mean rotational energy barrier⁴³ a/B , and the anisotropy ratio, b/a . Here $B = \hbar^2/2I$ is the molecular rotational energy constant, which is (7.356, 5.538, 3.709) meV for (H_2 , HD, D_2). Plotted in Fig. 9 are the transition energies from the ground-state to excited-state multiplets as a function of a/B . The lower panel corresponds to the isotropic rotor with $b=0$ and the upper panel to anisotropy

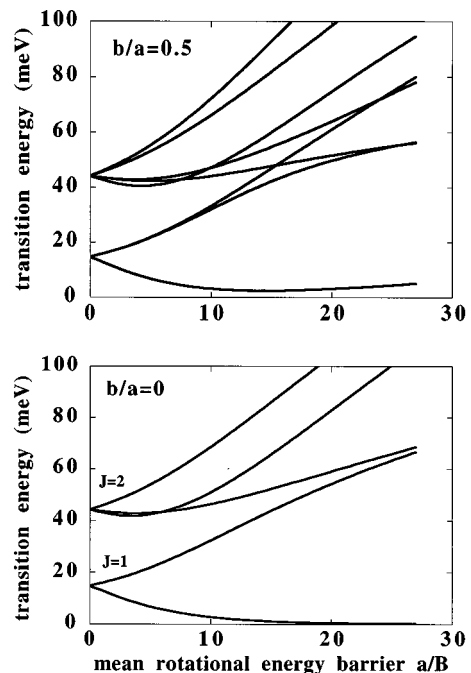


FIG. 9. Transition energies from the ground state to excited rotational states vs reduced rotational energy barrier. The lower panel corresponds to isotropic barrier and the upper panel is based on azimuthal anisotropy ratio $b/a=0.5$. The vertical axis energy scale corresponds to that for H_2 ; for HD and D_2 the energies are lower by a factor of 0.75 and 0.50, respectively. The same energy scale also enters into the rotational inertia parameter B on the horizontal axis, so that for the same barrier parameters, HD and D_2 are further to the right.

$b/a=0.5$. For nonzero b/a , the degeneracy between M and $-M$ states is split, as shown in the upper panel of the figure.

Although the rotational states represent at most only part of the hydrogen-molecule wave function, they already furnish guidance for the interpretation of the observed IINS spectrum (Fig. 1). If we assume that the lowest-energy IINS peak represents a rotational transition,⁴⁴ a constraint is imposed on allowable values of the rotational-barrier parameters a and b . Thus, in the vicinity of the trigonal site, $b \approx 0$, and the measured tunneling splitting of 1.4 meV implies $a/B \approx 13.5$. For HD the measured tunneling splitting of 0.4 meV implies $a/B \approx 19$, and so in the two cases the transition energy implies a barrier of 102 ± 10 meV, remarkably close to our calculated barrier. As described in Sec. IV A 3, however, the anisotropy increases for center of mass positions away from the trigonal site. The results in Fig. 9 show that the rotational-tunneling splitting of a rotor with given value of anisotropy parameter b has a lower bound as the mean rotational energy barrier a/B is varied. This minimum tunneling splitting is plotted as a function of b/a in Fig. 10. Based on the measured value (1.4 meV) of the tunneling splitting for H_2 , we find an upper bound on the anisotropy of about $b/a=0.3$. An even more stringent bound is obtained from the tunneling splitting for HD,⁴⁵ for which the transition energy (0.4 meV) requires an anisotropy of less than $b/a=0.15$. From this we conclude that a center-of-mass ground state localized in either of the two candidate sites

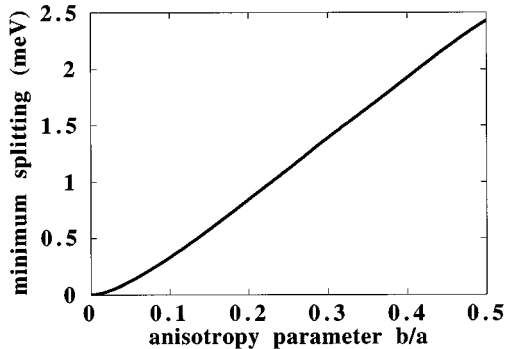


FIG. 10. Minimum tunneling splitting as a function of the azimuthal anisotropy parameter. Obtained from minima in curves such as those in Fig. 9.

from our calculated potential already appears to be incompatible with experiment, because of their higher rotational anisotropy. A more detailed consideration of center-of-mass states is given in the following sections.

A significant feature of the rotational spectra in Fig. 9 is the wide energy gap between the rotational-tunneling transition at 1–2 meV and the lowest “librational” mode transition between 30 and 50 meV (for $a/B \approx 10$ –20). The measured spectra in Fig. 1, on the other hand, show several peaks (at 2.7, 4, 11, and 22 meV) within this gap. (In the previous work of Stead *et al.*,^{3,4} only one peak in this energy range was identified). We now explore the possible relationship between these spectral peaks and center-of-mass state excitations.

2. Center-of-mass eigenstates

The potential for the center-of-mass motion, Eq. (11) is the superposition of the “direct” interaction $u(\mathbf{r})$ and the rotational and vibrational zero point energies, $E_{00}(\mathbf{r}) + E_0(\mathbf{r})$, respectively. The direct interaction was discussed in Sec. IV A 4. The variation of the zero-point energies over the unit cell is small compared with the variation in $u(\mathbf{r})$ and is therefore neglected. Instead of solving the molecular center-of-mass Schrödinger equation for the actual calculated potential $u(\mathbf{r})$, simplified, computationally tractable models are constructed, designed to capture the qualitative features of the states. Intermolecular interactions and the disordered domain structure of the Rb intercalants are neglected, because our aim is to assess the validity of the site-A crystal-field-state picture, which postulates states localized within individual cells of the $\sqrt{7} \times \sqrt{7}$ domains. The central issue is whether the “gap” transitions, such as those at 11 and 22 meV, can be attributed to center-of-mass state transitions, as suggested by Stead *et al.*^{3,4}

3. Rb-centered state

The potential given by Eq. (3) gives rise to a minimum of depth E_0 at radius x_0 surrounding the Rb intercalants. If x_0 were small enough that the contribution from neighboring alkali-metal intercalants (with midpoint distance $x = \sqrt{3}/2 = 0.866\dots$) were negligible, then at least the ground state would be localized in a ringlike state surrounding a Rb atom. In the harmonic approximation,

$$V_{\parallel}(r) = \frac{1}{2} m \omega_0^2 (r - r_0)^2. \quad (13)$$

The center-of-mass eigenstates for this potential can be labeled by radial quantum number n and (circular) angular momentum quantum number l . Since the harmonic oscillator frequency (19 meV) is greater than the well depth (9 meV), at most the $n=0$ state is localized, but bound states may exist with higher l . The approximate transition energies are

$$E_{0,l} - E_{0,0} \approx \hbar^2 l^2 / 2mr_0^2. \quad (14)$$

If we consider, hypothetically, $x_0 = 0.7$ ($r_0 = 5.0$ a.u.), transitions would occur at 0.15, 0.6, 1.4, 2.4, ... meV, and inverse-mass isotope scaling would be expected. For no values of x_0 in this range is there correspondence, however, between these predicted energies and experiment. The Rb-centered states therefore appear unlikely.

4. Bridge-centered and off-trigonal-site states

The LDFT calculations yield approximately $x_0 = 0.84$, which is close enough to half the intercalant separation for the wells from two neighboring alkali metals to overlap to form a deeper well in the “bridge” region. In this case the well forms an asymmetric two-dimensional harmonic oscillator, with roughly 25 meV frequency in the direction toward the alkali metals, and 4 meV frequency (very sensitive to the exact value of x_0) in the perpendicular direction. For x_0 slightly greater than $\sqrt{3}/2 = 0.866\dots$, this overlap well bifurcates into two wells with a small barrier between them at the bridge location; in fact we may already be seeing this in the full calculated potential of Fig. 6. In either case, such bridge-centered eigenstates would have center-of-mass transition energies in the range we are looking for and the correct isotope dependence, and it is tempting to identify the 22 meV peak with the calculated 25 meV oscillator frequency. However, this excited state energy seems too high to be localized in our calculated potential. Additional evidence against a bridge-centered ground state is the analysis in Sec. IV B, which indicates that the azimuthal anisotropy associated with a localized bridge-centered state is inconsistent with experiment.

For slightly larger values of the parameter x_0 there is a ring of minima surrounding the trigonal site, associated with the combined potentials of the three neighboring alkali metals. There is some evidence for this in our full calculated potential for the P21 polytype in Fig. 7. Equations (13) and (14) would again apply, but now the ring radius r_0 is reduced to around 1 a.u., and the transition energies from the ground state to states of different l would be 3.8, 15, 34, ... meV, within the energy region of interest. The rotational anisotropy may not be an issue in this case since the ground state has equal probability of being in positions with three different directions of anisotropy, so on average it should be roughly the same as the trigonal site itself, which has essentially no anisotropy. However, for these states the transition energies scale inversely with mass, and so again this result seems inconsistent with experiment.

5. Trigonal-site states

If the alkali- H_2 potential minimum parameter x_0 were close to 1 (due, for example, to overestimated quadrupole interactions in the LDFT calculation), the potential wells of three neighboring alkali metals would merge into a single well centered on the trigonal site. The resultant harmonic oscillator potential would be symmetric because of the three-fold symmetry there. The corresponding oscillator frequency estimated from Eq. (3) is close to 11 meV, and the intercell barrier at the bridge site is about 28 meV. The ground state and two excited states could be localized within such a well, giving transition frequencies at 11 and 22 meV, almost exactly matching IINS peak positions. Furthermore, the inverse square-root isotope effect for this model is in agreement with the experiments, as is the zero ground state rotational anisotropy.

Although such a center-of-mass potential is not directly supported by the LDFT calculations, it could arise from a slight modification of the fitted potential.

6. Extended states

Although we have thus far considered localized states, in the presence of perfect periodicity (the lattice of $\sqrt{7} \times \sqrt{7}$ unit cells) coherent Bloch states would be the formally correct representation. Consider a simplified model in which, instead of Eq. (3), the alkali-metal atoms are treated as hard disks. The states for this potential are delocalized; however, the bottlenecks between the disks appreciably narrow the bands. We note that similar potentials have been studied in the context of photonic bands in periodic dielectric arrays,⁴⁶ and the two-dimensional Sinai-billiard model.⁴⁷ We have calculated the eigenstates based on a technique developed in connection with the latter model.⁴⁷ It involves expanding the wavefunction in plane waves and determining the eigenvalues that are compatible with the zero boundary conditions at the disk surfaces. Guided by the potential in Fig. 6, we consider disks with radii 0.433 of the triangular lattice constant, which corresponds to 0.75 of the trigonal site-intercalant spacing. The first several eigenvalues for H_2 (starting with the ground state) are found to be 7.84, 15.89, 16.80, 21.88, and 25.3 meV. The corresponding bandwidths are of order 1 meV, although higher eigenstates have considerably larger bandwidths. These results confirm that the excluded volume associated with the disks appreciably narrows the bands and that at least the lowest energy transitions to resonant states above the potential barrier could produce relatively sharp peaks in the IINS spectrum. We note, however, that such states would have inverse-mass isotope-shift scaling, contrary to the experimental observation, which is a serious drawback of the hard-disk-array potential model.

C. Influence of intermolecular interactions

Clustering of the hydrogen molecules may occur at low temperatures, even for dilute filling, although there is at present no direct experimental evidence of this. It is therefore possible that the intermolecular interactions play an important role in the ground and excited states of this system, and in particular might be expected to enhance localization of the higher energy excited states. To treat the intermolecular interactions theoretically is a difficult many-body problem

(analogous, say, to solid hydrogen in a random external potential) and is not addressed in this article.

V. INTERPRETATION OF IINS SPECTRA

We discuss in this section the interpretation of the IINS spectrum. Since no selection rules are applicable, all excitations are in principle observable. In view of the large incoherent-neutron-scattering cross section of H, spectral peaks of primarily hydrogen character are expected to be prominent in H_2 and HD-doped intercalated graphite. Some host phonon spectral features⁴⁸⁻⁵¹ may also be visible. Since the first excited state as well as the ground state is populated at 15 K (see Sec. III D), higher excitations may give rise to doublets split by E_{H_2} or E_{HD} . In most of the following discussion, however, peak energies are interpreted as ground-to-excited-state differences.

A. 1.4 meV transition

The 1.4 meV peak is the sharpest inelastic spectral feature, as shown in the inset to Fig. 1. Its energy is well below the phonon density-of-states maxima of the binary stage-2 Rb GIC host⁴⁹ and thus represents a hydrogen feature. It is attributed to transitions between the lowest two rotational states⁴⁴ (“tunneling splitting”), as described in the preceding section. As mentioned earlier, its intensity is proportional to filling, whereas its position is insensitive to filling for $x < 0.8$.^{3,4} Further, values of the rotational barrier required by the isotropic (or weakly anisotropic) hindered-rotor model to yield the observed tunneling splitting for H_2 and HD ($a \approx 100$ meV) are in close agreement with each other, and with our LDFT calculations. These results all lend support to the crystal-field-state picture.³ Incidentally, the tunneling-splitting in the D_2 -doped system (less than 0.1 meV) is below the experimental resolution.

B. 2.7 and 4.0 meV transitions

The 2.7 and 4.0 meV transitions, not previously observed, may represent host features. Simulations for stage-2 Rb GIC (Ref. 50) showed a phonon DOS peak associated with in-plane Rb-intercalant modes centered at 4.2 meV, in close agreement with experimental observations.⁵¹ The 4.0 meV peak seen in Fig. 1 may plausibly be identified with the 4.2 meV phonon peak in Rb GIC, with the peak shifted slightly owing to the presence of the hydrogen molecules. Consistent with this interpretation is the absence of an isotope shift in the corresponding peak for $C_{24}Rb(HD)_x$.

The 2.7 meV transition may be (i) a subfeature of the manifold including the 4.0 meV peak, (ii) another manifestation of the 4.0 meV feature, shifted by E_{H_2} , corresponding to orthohydrogen, or (iii) an in-plane molecular-center-of-mass vibrational state. The feature at 1.5 meV in $C_{24}Rb(HD)_x$ may represent (iii), shifted by the isotope effect. These energies (2.7 and 1.5 meV) appear sufficiently small to be consistent with the shallow in-plane potential wells predicted by the LDFT calculations, and could be associated with transitions between the ringlike states of Sec. IV B.

C. 11 and 22 meV transitions

The transition at 22 meV was previously observed by Stead *et al.*^{3,4} The splitting of the 11 meV transition in C₂₄Rb(H₂)_x, may be associated with orthohydrogen. It is tempting to interpret the 11 and 22 meV transitions as the first two excitations of harmonic-oscillator-like states, because of the approximately inverse square-root isotope effect (Sec. III) and the integral ratio of the transition energies. On the other hand, the frequency of the (LDFT-predicted) out-of-plane potential is too high to be relevant to these transitions, whereas the high excitation energies are difficult to reconcile with the shallow in-plane potential wells. We note, however, that the extended excited states may be sufficiently narrow to match the observations. Furthermore, another possible scenario is that the LDFT calculations overestimate the attractive part of the H₂-Rb interaction, as discussed in Sec. IV B 5; a trigonal-site centered harmonic potential may then produce an almost perfect match to the experimental transition energy and isotope shift, as well as the inferred rotational anisotropy. In any case, the 11 and 23 meV transition energies are of the same order of magnitude as transitions predicted within several models of the H₂ center-of-mass motion, so it is not unreasonable to attribute the transitions to center-of-mass motion, even if the precise states have not been established.

D. 32 meV transition

The 32 meV transition is distinguished from those at 11 and 22 meV by its minute isotope shift, which seems to preclude assignment as a third transition in that sequence, and the small integrated intensity. This might suggest appreciable host participation in this mode, although the highest energy phonon density-of-states features attributed to alkali-metal intercalants⁴⁹ are in the range of 13 meV. Also worthy of consideration is the possibility that this mode is the second rotational (first librational) transition of the H₂ molecule. With an isotropic-hindered-rotor-model rotational barrier of $a/B \approx 14$ ($a \approx 100$ meV), the second rotational transition occurs at 39 meV (Fig. 9). This is considerably larger than the experimental value; however, it is possible that nonsinusoidal contributions to the rotational potential, as well as rotational-translational coupling, significantly shift the observed transition. The observed HD to H₂ ratio of transition energies of 0.95 is consistent with the predicted ratio of 0.94.

The small integrated intensity indicates a small matrix element. General considerations suggest that librational transitions have smaller matrix elements than those associated with center-of-mass motion, which provides additional support for the assignment of this mode to the librational transition.

The next highest predicted rotational transition (which corresponds to $J=2$, $M=1$) for the isotropic hindered-rotor model is at 49 meV. The experimental data, however, do not show any distinct feature in this energy range, or at higher energies. Either small matrix elements and/or wide bandwidths for these states may make them unobservable.

E. 44 meV transition

Model calculations for both librational and out-of-plane vibrational modes yield energies in the vicinity of the ob-

served value of 44 meV. The observed isotope shift ratio of 0.82 between HD and H₂, however, is consistent with a harmonic oscillator transition and cannot easily be reconciled with the isotope shift ratio of 0.94 predicted for the librational mode.

Although 44 meV is again close to a multiple of the apparent 11 meV in-plane oscillator frequency, the LDFT calculations also predict a perpendicular center-of-mass vibrational frequency of 45 meV, and the matrix-element argument (as well as the greater intensity of the 44 meV peak than the 32 meV peak) suggests that the observed transition is indeed associated with this out-of-plane vibrational motion.

F. Transitions at higher fillings

A remaining issue is the identity of site *B*. None of the $\sqrt{7} \times \sqrt{7}$ sites appears to have the high rotational barrier called for by the low observed tunneling splitting,^{3,4} and therefore site *B* is most likely located in a higher alkali-metal-ion-density region of the system, which becomes populated only after most of the energetically favorable *A* sites are filled.

VI. DISCUSSION

A primary motivation of this work was to assess to what extent IINS spectra for C₂₄Rb(H₂)_x (and related isotopically substituted systems) provide a detailed signature of the local environment surrounding the hydrogen molecules. If the crystal-field-state picture could be made more quantitative, it would lend confidence to the application of IINS spectroscopy as a nanostructural probe of other hydrogen-doped porous systems, such as molecular sieves.

The interpretation in the earlier work by Stead *et al.*^{3,4} focused on the rotational transitions and did not consider center-of-mass excitations. It was found that the isotropic-hindered-rotor model (Sec. III) could apparently account for several of the observed IINS peak positions, whereas some other possible crystal-field symmetries, for example, tetragonal,⁵² yield splittings between rotational-tunneling and fundamental-librational lines ($JM=10$ and 11) much larger than experiment. No direct theoretical justification of the isotropic-hindered-rotor model was available, however.

The LDFT calculations in the present study suggest that the isotropic-hindered-rotor model is essentially correct, although the model should be generalized to include a small azimuthal anisotropy, the consequences of which are considered in the Appendix and in Sec. III. On the other hand, several transition peaks identified in the earlier work^{3,4} were not reproduced in the present IINS measurements. Furthermore, the 44 meV peak, previously attributed to the fundamental librational transition, appears more likely associated with an out-of-plane vibrational mode, based on the isotope shifts, as well as the LDFT calculations. We tentatively assign the fundamental librational transition to the narrower but weaker 32 meV peak. Overall, therefore, although the hindered-rotor model is now on a firmer theoretical footing, the role of librational transitions in the observed IINS spectra is not as clear as it seemed.

Particular attention was given in the present work to the

spectral peaks that could not be identified with rotational transitions, namely, those features between the rotational tunneling peak at the 1.4 and 32 meV peak. Of these peaks, the ones at 11 and 22 meV are perhaps most critical. They show an inverse square-root (harmonic-oscillator like) isotope shift in the spectra for both HD and D₂ and therefore represent hydrogenic rather than host features. Calculations based directly on the LDFT potential, however, are unable to reproduce all the essential features of these transitions (transition energy, isotope shift, and the ground-state rotational anisotropy). A modification of a potential model fitted to the LDFT calculations suggests that the explanation may be a harmonic potential well centered on the trigonal site, resulting from the superposition of the potential for neighboring alkali metals.

We have mentioned in Sec. III that our single-particle-approximation theoretical treatment, although a necessary starting point, neglects several many-body effects (phononic, electronic, and intermolecular) that may be important. For example, since the predicted single-particle-approximation bandwidths, of order 1 meV, are of the same order as the measurement temperature (15 K), localization of the ground state is likely. The localization of the excited states at 11 and 22 meV, for which at least the second is likely to be higher than the single-particle-approximation barriers to migration, is more difficult to judge. The role of the intermolecular interactions may be important for a proper description of the localization of the center of mass excited states. Even with these uncertainties about the center of mass states, the correlation between calculated and observed spectroscopic features reinforces the promise of this kind of hydrogen spectroscopy as a nanostructural probe of porous materials.

ACKNOWLEDGMENTS

L.H.Y. was supported at Lawrence Livermore National Laboratory by the U.S. Department of Energy under Contract

No. W-7405-ENG-48. A.P.S., R.B., M.M., and F.R.T. were supported at Argonne National Laboratory by the U.S. Department of Energy under Contract No. W-31-109-ENG-38. Most of the computational work was performed at the National Energy Research Supercomputer Center, Lawrence Livermore National Laboratory. Calculations were also performed on the CM-200 at the Minnesota Supercomputer Center.

APPENDIX: THE ANISOTROPIC ROTOR MODEL

For a three-dimensional rotor described by coordinates θ , ϕ , the free eigenstates are the spherical harmonics $Y_{lm}(\theta, \phi)$ with energy eigenvalues $\hbar^2 l(l+1)/2I$, where I is the moment of inertia of the rotor. The Hamiltonian matrix elements in the presence of a rotational potential $w(\Omega)$ can be written

$$H_{lm,l'm'} = \hbar^2 l(l+1)/(2I) \delta_{ll'} \delta_{mm'} + \langle Y_{l'm'} | w(\Omega) | Y_{lm} \rangle, \quad (\text{A1})$$

and the corresponding states are obtained by diagonalization of the resultant matrix. The simplest way to evaluate the matrix elements of the potential is to rewrite our angular potential $w(\Omega) = \sin^2 \theta [a + b \cos(2\phi)]$ as a sum of spherical harmonics:

$$w(\Omega) = a \left[\frac{2}{3} \sqrt{4\pi} Y_{00}(\theta, \phi) - \frac{4}{3} \sqrt{\pi/5} Y_{20}(\theta, \phi) \right] + (b/2)(32\pi/15)^{1/2} (Y_{22} + Y_{2-2}). \quad (\text{A2})$$

Then the matrix elements are simple triple integrals of spherical harmonic functions, which can be evaluated in terms of Clebsch-Gordan coefficients:

$$\begin{aligned} \langle Y_{l'm'} | w(\Omega) | Y_{lm} \rangle = & \frac{2}{3} [(2l+1)/(2l'+1)]^{1/2} [a \delta_{ll'} \delta_{mm'} - a \cdot \{ C(l,2,l+2;m,0,m) C(l,2,l+2;000) \delta_{mm'} \delta_{l'l+2} \\ & + C(l,2,l;m,0,m) C(l,2,l;000) \delta_{mm'} \delta_{ll'} + C(l,2,l-2;m,0,m) C(l,2,l-2;000) \delta_{mm'} \delta_{l'l-2} \} \\ & + (3/2)^{1/2} b \{ C(l,2,l+2;m,2,m+2) C(l,2,l+2;000) \delta_{m',m+2} \delta_{l',l+2} \\ & + C(l,2,l+2;m,-2,m-2) C(l,2,l+2;000) \delta_{m',m-2} \delta_{l',l+2} + C(l,2,l;m,2,m \\ & + 2) C(l,2,l;000) \delta_{m',m+2} \delta_{l',l} + C(l,2,l;m,-2,m-2) C(l,2,l;000) \delta_{m',m-2} \delta_{l',l} \\ & + C(l,2,l-2;m,2,m+2) C(l,2,l-2;000) \delta_{m',m+2} \delta_{l',l-2} + C(l,2,l-2;m,-2,m-2) \\ & \times C(l,2,l-2;000) \delta_{m',m-2} \delta_{l',l-2} \}]. \end{aligned} \quad (\text{A3})$$

We can immediately simplify somewhat by noting that nonzero matrix elements appear only between states differing in l or m by multiples of 2, so there is actually a conserved parity-type quantum number for l and for m : $p=l \bmod 2$ and $q=m \bmod 2$, leading to four disjoint subblocks in the Hamiltonian, with $p=0$ or 1 and $q=0,1$. The Clebsch-Gordan coefficients $C(\dots)$ can be readily evaluated numerically by one of the standard iteration schemes,

although the ones we needed here (those with $\Delta l = \pm 2, 0$ and $\Delta m = \pm 2, 0$) can be obtained from standard tables.⁵³ In calculating the eigenenergies shown in Figs. 9 and 10 we performed exact diagonalizations of the matrices for fixed p and q values, including all free rotor states with $l < l_c$. By comparing results for different values of the angular-momentum cutoff, we found excellent convergence for $l_c = 12$.

- *Present address: Chemistry Department BG-10, University of Washington, Seattle, WA 98195.
- ¹A. D. Novaco and F. J. Milford, *J. Low-Temp. Phys.* **3**, 307 (1970).
 - ²R. Moreh, S. Melloul, and H. Zabel, *Phys. Rev. B* **47**, 10 754 (1992).
 - ³W. J. Stead, P. Meehan, and J. W. White, *J. Chem. Soc. Faraday Trans. 2* **84**, 1655 (1988).
 - ⁴W. J. Stead, I. P. Jackson, J. McCaffrey, and J. W. White, *J. Chem. Soc. Faraday Trans. 2* **84**, 1669 (1988).
 - ⁵*Gas-Surface Interaction and Physisorption*, edited by G. Benedek, V. Celli, M. W. Cole, F. Toigo, and J. Weare [*Surf. Sci.* **148**, 1 (1984)].
 - ⁶J. M. Gottlieb and L. W. Bruch, *Phys. Rev. B* **40**, 148 (1992).
 - ⁷J. M. Nicol, J. Eckert, and J. Howard, *J. Phys. Chem.* **92**, 7117 (1988).
 - ⁸G. J. Kellogg, J. W. White, K. Herwig, and P. E. Sokol, *J. Chem. Phys.* **93**, 7153 (1990).
 - ⁹D. L. Freeman, *J. Chem. Phys.* **62**, 4300 (1975).
 - ¹⁰A. D. Novaco, *Phys. Rev. B* **46**, 8178 (1992).
 - ¹¹G. R. S. Naylor and J. W. White, *J. Chem. Soc. Faraday Trans. 2* **83**, 3447 (1987).
 - ¹²R. Clarke, J. N. Gray, H. Homma, and M. J. Winokur, *Phys. Rev. Lett.* **47**, 1407 (1981).
 - ¹³M. J. Winokur and R. Clarke, *Phys. Rev. Lett.* **54**, 811 (1985).
 - ¹⁴H. Seong, S. Sen, T. Cagin, and S. D. Mahanti, *Phys. Rev. B* **45**, 8841 (1992).
 - ¹⁵H. Seong, S. D. Mahanti, S. Sen, and T. Cagin, *Phys. Rev. B* **46**, 8748 (1992).
 - ¹⁶J. W. White (private communication).
 - ¹⁷The excitation from the ($J=0$) to the ($J=1, M=0$) rotational state (Refs. 3 and 4) is referred to as the rotational-tunneling transition.
 - ¹⁸Measurements on single (or highly oriented) crystals would be desirable, however, achieving homogeneous hydrogen filling of monocrystals is difficult.
 - ¹⁹Hydrogen doping was performed at 100 K. The quasielastic line-width decreases markedly at about 50 K, which signals the freezing of molecular diffusive motion.
 - ²⁰K. G. Petzinger, *Phys. Rev. B* **26**, 6530 (1982).
 - ²¹P. Hedegard, *Phys. Rev. B* **35**, 533 (1987).
 - ²²H. Krimmel, I. Schimmele, C. Elsaesser, and M. Faehle, *J. Phys. Condens. Matter* **6**, 7679 (1994).
 - ²³Bound states occur in two (but not in three) dimensions for an infinitesimally small attractive potential strength $V_0 a^2$, where a is the size of the potential well of depth V_0 .
 - ²⁴P. W. Anderson, *Phys. Rev.* **108**, 1492 (1958).
 - ²⁵T. Holstein, *Ann. Phys. (N.Y.)* **8**, 343 (1959).
 - ²⁶R. C. Casella, *Phys. Rev. B* **27**, 5943 (1983).
 - ²⁷S. Chung, N. Holter, and M. W. Cole, *Phys. Rev. B* **31**, 6660 (1985).
 - ²⁸R. Benedek, A. P. Smith, and L. H. Yang, *Phys. Rev. B* **49**, 7786 (1994).
 - ²⁹N. Troullier and J. L. Martins, *Phys. Rev. B* **43**, 1993 (1991).
 - ³⁰L. H. Yang, A. P. Smith, R. Benedek, and D. D. Koelling, *Phys. Rev. B* **47**, 16 101 (1993).
 - ³¹A. P. Smith, R. Benedek, F. R. Trouw, and L. H. Yang, *Phys. Rev. B* **49**, 5050 (1994).
 - ³²M. Teter, M. Payne, and D. G. Allan, *Phys. Rev. B* **40**, 12 255 (1989).
 - ³³R. Benedek, L. H. Yang, C. Woodward, and B. I. Min, *Phys. Rev. B* **45**, 2607 (1992).
 - ³⁴C.L. Fu and K. M. Ho, *Phys. Rev. B* **28**, 5480 (1983).
 - ³⁵D. E. Nixon and G. S. Parry, *J. Phys. D* **1**, 291 (1968).
 - ³⁶D. Fristot, A. Charlier, M. F. Charlier, L. Lang, and S. Doyen-Lang, *J. Phys. Condens. Matter* **3**, 5323 (1991).
 - ³⁷K. Watanabe, T. Kondow, M. Soma, T. Onishi, and K. Tamaru, *Proc. R. Soc. London Ser. A* **333**, 51 (1973).
 - ³⁸R. Benedek, A. P. Smith, and L. H. Yang (unpublished).
 - ³⁹B. Firey, F. W. de Wette, E. De Rouffignac, and G. P. Alldredge, *Phys. Rev. B* **28**, 7210 (1983).
 - ⁴⁰The numerical values of the fitted parameters are $A=309.867$ meV, $\alpha=3.13859$, $C=214.057$ meV, and $D=27.9986$ meV, where the unit of length is $\sqrt{7}$ times the carbon-carbon bond length.
 - ⁴¹I. S. Silvera and V. V. Goldman, *J. Chem. Phys.* **69**, 4209 (1978).
 - ⁴²T. B. MacRury and J. R. Sams, *Mol. Phys.* **19**, 337 (1970).
 - ⁴³When $b=0$, the variable a is equivalent to $2V_0$ in Ref. 4.
 - ⁴⁴That the lowest-energy peak represents a rotational transition can in principle be demonstrated in the following way (J. Eckert, private communication). By holding a specimen for several days at low enough temperature (≈ 1 K) that the Boltzmann ratio e/g (cf. Sec. III D) is essentially zero, the orthohydrogen originally present would all convert to parahydrogen if the excited state is translational, but only partially convert for a rotational excited state; this follows from the assumption that coupling of translational modes to the lattice would be strong and result in essentially instantaneous conversion, whereas coupling to rotational degrees of freedom would be weak, leading to relatively slow conversion. Under these circumstances, incomplete conversion would be signaled by observation of the lowest-energy (rotational-tunneling) peak in neutron energy gain (transition from $J=1$ to $J=0$) as well as in energy loss (transition from $J=0$ to $J=1$). This test, however, was not performed in the present work.
 - ⁴⁵To adapt Fig. 9 to HD molecules, both the ordinate and the abscissa axes must be scaled appropriately by the moment of inertia.
 - ⁴⁶K. M. Ho, C. T. Chan, and C. M. Soukoulis, *Phys. Rev. Lett.* **65**, 3152 (1990).
 - ⁴⁷S. Sridhar and E. J. Heller, *Phys. Rev. B* **46**, 1728 (1992).
 - ⁴⁸H. Zabel, in *Graphite Intercalation Compounds I*, edited by H. Zabel and S. Solin (Springer, Berlin, 1992), p. 101.
 - ⁴⁹R. Al-Jishi and G. Dresselhaus, *Phys. Rev. B* **26**, 4523 (1982).
 - ⁵⁰H. Seong and S. D. Mahanti, *Phys. Rev. B* **49**, 5042 (1994).
 - ⁵¹W. A. Kamitakahara and H. Zabel, *Phys. Rev. B* **32**, 7817 (1985).
 - ⁵²D. Smith, *J. Chem. Phys.* **68**, 3222 (1978).
 - ⁵³E. U. Condon and G. H. Shortley, *The Theory of Atomic Spectra* (Cambridge University Press, Cambridge, 1951), p. 76.